Measuring liquid film thickness in annular two-phase flows by cold neutron imaging

Author(s):
Zboray, Robert; Prasser, Horst-Michael

Publication date:
2013-09

Permanent link:
https://doi.org/10.3929/ethz-b-000073824

Originally published in:
Experiments in Fluids 54(9), https://doi.org/10.1007/s00348-013-1596-1

Exp Fluids (2013) 54:1596
DOI 10.1007/s00348-013-1596-1

RESEARCH ARTICLE

Measuring liquid film thickness in annular two-phase flows by cold neutron imaging

R. Zboray · H.-M. Prasser

Received: 3 May 2013 / Revised: 23 July 2013 / Accepted: 28 August 2013 / Published online: 13 September 2013

Abstract An overview of a measurement method for liquid film thickness in annular flows based on cold neutron imaging is given here. Neutron imaging being a non-intrusive, contactless method is attractive option for two-phase flow investigations offering an excellent contrast. It can provide with information at a high spatial resolution on the flow structure, like the thickness of the liquid film in annular flows. The method has been optimized, and its performance, regarding bias, statistical accuracy, upper and lower detection limits, has been thoroughly quantified using computational tools and measurement results. The technique has been developed based on nuclear fuel bundle models; however, it is applicable practically to annular flows in any arbitrary flow channel geometry of interest.

Abbreviations

cps	Counts per second
CCD	Charge coupled device
CNR	Contrast-to-noise ratio
FBP	Filtered back projections
FOV	Field of view
LFT	Liquid film thickness
LFS	Liquid film sensor
LSF	Line spread function
MC	Monte Carlo simulation
SNR	Signal-to-noise ratio
PSF	Point spread function
ROI	Region of interest
var	Variance

Latin symbols

A	Area
D	Dose or diameter
Gd	Gadolinium
I	Intensity
J	Superficial velocity
L	Length
Li	Lithium
V	Volume
p	Pixel gray value
pr	Projection
R	Radon transform
t	Distance

Greek symbols

β	Gas volume flow fraction
ε	Liquid holdup
σ	Standard deviation
ϕ	Polar angle
θ	Projection angle
Σ	Macroscopic neutron interaction cross-section

Subscript

emp	Empty
g	Gas
l	Liquid

R. Zboray (✉) · H.-M. Prasser
Laboratory for Thermal-hydraulics, Nuclear Energy and Safety Department, Paul Scherrer Institute, 5232 Villigen, Switzerland
e-mail: robert.zboray@psi.ch

H.-M. Prasser
e-mail: prasser@psi.ch

H.-M. Prasser
Laboratory for Nuclear Energy Systems, Department of Mechanical and Process Engineering, ETH Zurich, Sonneggstrasse 3, 8092 Zurich, Switzerland

1 Introduction

We introduce and thoroughly discuss here a method for liquid film thickness (LFT) measurement in annular flows using cold neutron tomography.

Annular flow is one of the most frequently observed two-phase flow patterns in industrial applications like evaporators, heat exchangers or in many other gas–liquid two-phase systems. Annular flow is characterized by the presence of a continuous liquid film flowing on the channel wall surrounding a central gas core laden with liquid droplets entrained from the liquid film. The gas–liquid interface is highly dynamic with very erratic waves traveling on it. The literature usually distinguishes between large disturbance waves and relatively small-wavelength and small-amplitude ripple waves traveling at much lower velocity compared to the velocity of the disturbance waves and of the gas phase (Hewitt and Hall-Taylor 1970; Azzopardi 1997). Depending on the actual application, different aspects of the annular flow might be of interest. For many cases, the LFT is of primary importance for the thermal hydraulic behavior of the equipment like in nuclear fuel bundles. Waves in the liquid film impact the pressure drop over the channel, which can be interesting for design considerations of the two-phase equipment. The atomization of the large disturbance waves by the turbulent gas core is believed to be the main source of droplet entrainment into the core of the annular flow (Hewitt and Hall-Taylor 1970). Fully developed droplet entrainment is known as equilibrium entrainment and is described by equal rates of droplet entrainment from the film and of deposition of droplets onto the film. At low gas and/or liquid velocities, there is no evidence of entrainment, and the criteria for the onset of droplet entrainment are well described by Ishii and Grolmes (1975). Understanding of droplet entrainment and the entrained liquid fraction can be also important for many applications. The entrainment/deposition rates depend on droplet-velocity distribution, which is dependent on the droplet size distribution (Fore and Dukler 1995; Trabold et al. 1998; Fore et al. 2002)

We have developed our method in the context of nuclear fuel bundle research where the phenomenon of boiling crises caused by the dryout of the liquid film is of central interest (Lahey and Moody 1993); therefore, we focus on a technique measuring the LFT in annular flow. Nevertheless, the method could be applied for other settings as well, where liquid films are present like, e.g., the interaction of sprays and solid surfaces in injection engines, gas turbines, spray cooling or coating.

By far the most popular methods for measuring the LFT are by conductance or capacitance (e.g., Fukano 1998; Han et al. 2006). Non-intrusive versions incorporate electrodes mounted flush to the wall (e.g., Fukano 1998; Feldhaus et al. 2002). In this context, Damsohn and Prasser (2009a, b) have developed a conductivity-based liquid film sensor (LFS) capable of a 10 kHz sampling rate at a spatial resolution of 2 mm. They investigated LFT and wave behavior in fuel bundle model subchannel geometry for different gases and with various functional spacer vanes (Damsohn and Prasser 2010). Other non-intrusive methods mostly involve optical techniques (Azzopardi and Zaidi 1999; Fore et al. 2002) or ultrasonic techniques (Kamei and Serizawa 1998).

As for non-intrusive imaging techniques involving radiation, X-ray and gamma-ray radiography and tomography have been for some time the first choice both for general two-phase flow research (e.g., Misawa et al. 2004; Stahl and Rudolf von Rohr 2004) and for nuclear fuel bundle investigations (e.g., Kok et al. 2001; Neykov et al. 2005). Zboray et al. (2011b) have investigated annular flows in a fuel bundle model using ultra-fast X-ray tomography delivering very high frame rates of several kframes/s being able to capture also most of the dynamics of the 2-phase flow. The spatial resolution was, however, limited somewhat above 1 mm being too coarse for thin liquid films characterizing the annular flows shown here.

Neutron imaging is still exotic in this field though it started to be increasingly applied in the last decade as it offers several advantages compared to the aforementioned techniques like:

- non-transparent channels can be investigated unlike with optical-based techniques,
- imaging through thick(er) metal housings and structures, posed by the geometry or by high pressure/temperate flow conditions, is possible, where gamma-ray- and X-ray-based methods would deliver much poorer contrast, if applicable at all,
- it can be applied in very complicated, curved geometries with a multitude of characteristic length scales, for which conductance-based sensors would be really problematic due to difficulty of installation or optical-based techniques due to obstruction of the view.
- it delivers information in 3D, which is not the case for many of the aforementioned techniques.

Using neutron imaging for fuel bundle research, Takenaka et al. have performed a number of studies (Takenaka et al. 1998; Takenaka and Asano 2005) and compared the performance of fast and thermal neutron imaging (Takenaka et al. 1999). Lim et al. (2005) performed high-frame rate thermal neutron radiography on a model fuel bundle. Mishima et al. (1999) have examined a model of two adjacent subchannels of a high conversion light water reactor (HCLWR) tight-lattice fuel bundle using neutrons. Kureta (2007a, b) and Kureta et al. (2008) have performed

comprehensive investigations on a triangular, tight-lattice fuel bundle model using thermal neutron tomography. They examined different flow regimes including annular flow but neither they nor the aforementioned authors tried to characterize LFT distributions in details.

We have developed and investigated the technique by imaging different models of nuclear fuel bundle geometries representing a section of a full bundle. The neutron imaging experiments on annular flows in these models have been performed at the ICON beam line of the spallation neutron source (SINQ) at the Paul Scherrer Institute, Switzerland. First, the geometries and the annular flow parameters are illustrated briefly through some examples. Then, the imaging setup and its modalities are introduced. After that, the paper thoroughly analyzes the performance of the technique for determining the LFT distribution.

2 Experimental facility and imaging setup

2.1 The two-phase flow loop incorporating the different fuel bundle models

The two-phase loop comprises a flow channel representing the actual geometry of the fuel bundle under investigation, complemented by a recirculation auxiliary system closing the two-phase flow loop operated at near ambient pressures and ambient temperatures. A photo of the flow channel and a scheme of the loop are given in Fig. 1. The two-phase mixture of air and water is created at the bottom of the channel, and it exits at the top of it into a tank, where the air is left to egress while the water is recycled by a pump. The air flow is measured by a rotameter (accuracy is about 2 % of range, 0–120 Nm^3/h), while the water flow is measured by a vortex flow meter (accuracy 0.75 % of range, 0–200 l/h). The water is pumped back to the test section by a frequency-controlled pump, whose speed is controlled based on the reading of the vortex flow meter. The absolute pressure in the channel is measured at its base near the air inlet (accuracy ±0.05 bar). Flexible inlet and outlet hosing allows the entire channel to rotate 180° around its vertical axis on a motor-actuated turntable during the course of a tomographic measurement.

Three different bundle geometries modeled in these investigations are shown in Fig. 2.

Each channel model comprised a thin-wall (3 mm thickness) upper section (shown in Fig. 2) and a thick-wall lower section. The channel is constructed entirely out of Anticorodal-110® (EN AW-6082). This aluminum alloy is chosen for its corrosion resistance and welding properties, but most importantly, it is quite transparent for neutrons, ensuring the majority of neutron flux is attenuated by the water film inside the test section and not by the channel walls. Always, the upper, thin-wall section, which is 45 cm tall, has been imaged as is shown in Fig. 1. It also hosts the spacers if they are present. Below the thin-wall section,

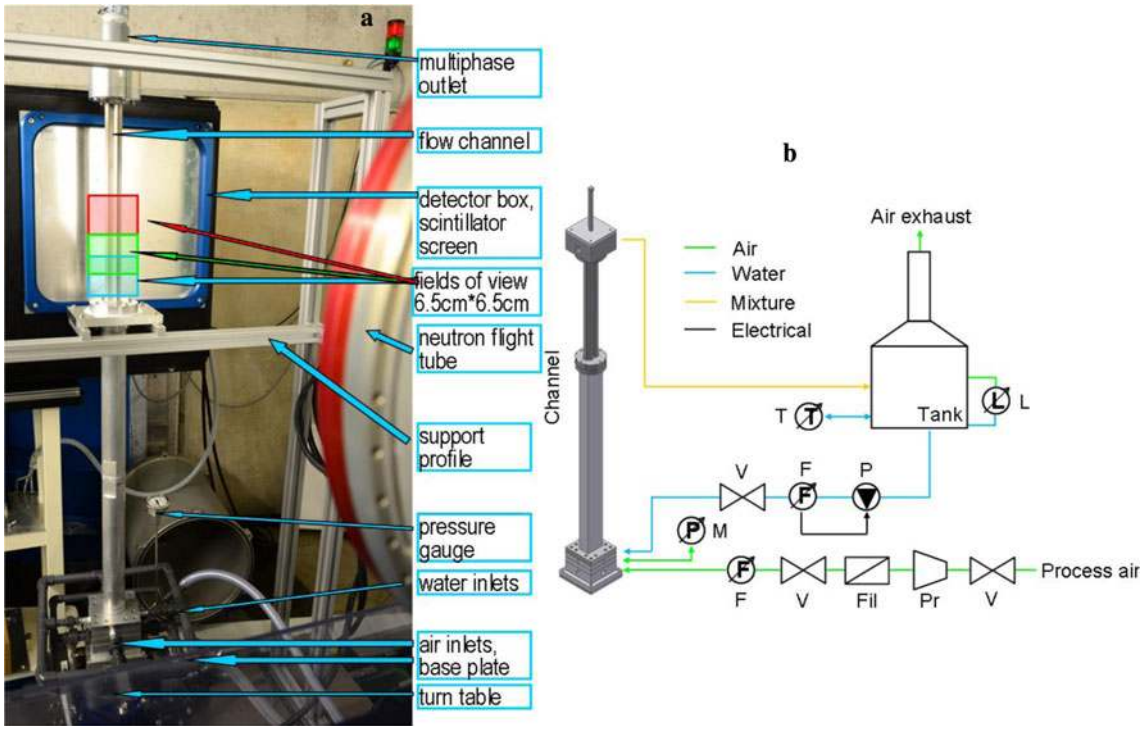

Fig. 1 Photo of the two-phase flow channel at the neutron beam line (**a**) and a schematic of the complete two-phase loop (**b**)

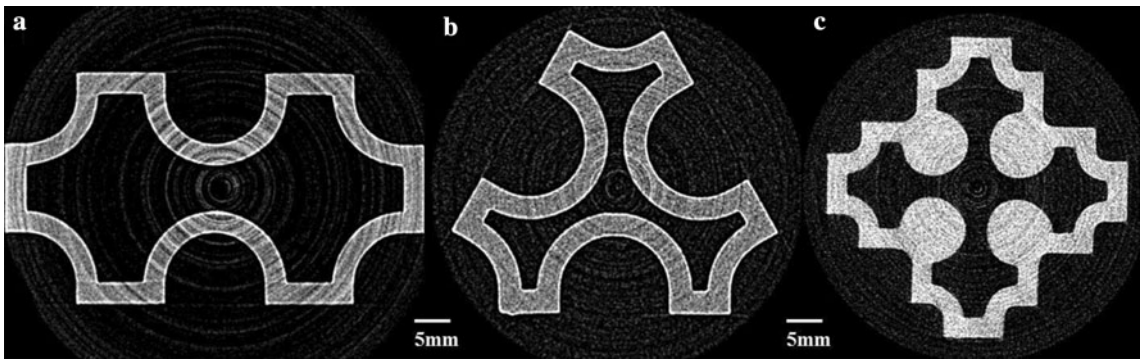

Fig. 2 Reconstructed cross-sections of the empty flow channels illustrating the different geometries used in these studies comprising a double subchannel model of a rectangular fuel lattice (**a**), a triangular lattice model with 4 subchannels (**b**) and a rectangular with 5 neighboring subchannels

connected by a flange, is an 80.5-cm-long segment with thicker outer walls and the same tight-lattice subchannel geometry inside.

The base of the channel comprises a base plate adapter for connection to the turntable, four air inlets, a flow stratifier and four water inlets (one each side) above that (see Fig. 1), all this over 8 cm in height. The water inlet piece is designed specifically to inject the liquid at the walls using beveled edges such that the flow is already near-annular at the inlet. The flow is provided approximately 90 cm upstream to develop before reaching the spacer vanes.

2.2 The cold neutron imaging setup at the ICON beam line

The imaging of the different flow channels has been performed at the cold neutron beam line, ICON, at the SINQ spallation neutron source at the Paul Scherrer Institute, Switzerland (Kaestner et al. 2011). SINQ utilizes a high-intensity, 590-MeV proton beam hitting a lead target head. An average proton beam current of about 1.5 mA delivers a neutron flux at our measuring position at the ICON beam line of about 4×10^6 $cm^{-2}s^{-1}$. The majority of the neutrons have energies significantly below 0.025 eV, i.e., in the cold range (see, e.g., Kaestner et al. 2011).

The imaging optics consisted of a 1,024 × 1,024 pixels, cooled ANDOR DV-434 CCD camera with 16-bit dynamic range. The camera is equipped typically with a 100-mm Nikon lens at a high relative aperture setting of f/2.0–f/2.8 focusing on a scintillator/converter screen through a mirror at 45° angle. A field of view (FOV) of about 6×6 cm^2–9×9 cm^2 can be achieved depending on the settings corresponding to a pixel size of about 60–90 μm/pixel, respectively. The camera and mirror are placed in a light-tight box, whose only opening is covered by the scintillation screen. A reasonably high L/D (L = collimator length, D = beam aperture diameter) ratio of about 604 is achieved using a 20-mm beam aperture as a good compromise enabling low beam divergence at still reasonable neutron fluxes and exposure times.

The scintillator screens are thin layers with a granular structure painted on a substrate containing a neutron-converting component either Li^6 or Gd. The former converts neutrons into to a triton and an alpha particle, the latter into conversion electrons (see, e.g., Crow 2009). These reaction products create light in the scintillating component of the screen, which is ZnS(Ag) in case of Li^6 and Gd_2O_2S(Tb) (termed as Gadox) in the other case. The most important properties of the converter screens are the inherent blur impacting the spatial resolution and the sensitivity imposing the necessary exposure times. The main characteristics of the different screens and the settings as we have tested them are summarized in Table 1. It shows that the Li-based screens have a higher sensitivity mainly due to their higher thickness enabling lower exposure times for the same signal-to-noise ratio (SNR). However, higher thickness diminishes the spatial resolution as the reaction products are quite energetic (Crow 2009) and have relatively long

Table 1 Summary of the different imaging settings that have been tested during the different test campaigns including scintillator/converter screen types and properties, typical exposure times used and screen to object distances

Screen type:	Li^6/ZnS:Ag		Gadox
Thickness (μm)	100	50	20
Sensitivity (cps/mA beam)[a]	515.8	226.5	95.35
Average screen to object distance (cm)	17	17	2.5
Typical exposure times/projection (s)	30–40	40–60	100
Spatial resolution (μm)	385	316	245

The last row lists the spatial resolution of the imaging setup including geometrical unsharpness, screen blur and blur by the optics and is obtained from measured edge responses to a Gd strip attached to the object

[a] Indicative, taken from Kaestner et al. (2011)

ranges in the screen material (for the triton $\sim$50 μm) contributing significantly to the inherent blurring of the localization of the point of neutron impact. The very high neutron absorption cross-section of Gd enables decreasing the layer thickness down to 10–20 μm retaining still reasonable sensitivities (see Table 1). Furthermore, the low-energy conversion electrons from the Gd reaction have much lower ranges (10–20 μm), both effects contributing to a better spatial resolution. The disadvantage of the Gadox screen compared to Li-based ones is the low light output due to the low energy of the conversion electrons. For details, see Kardjilov et al. (2011)

Another contribution to overall blur is a geometrical unsharpness, a penumbra effect due to the slight divergence of the neutron beam. This can be minimized by decreasing the distance between the channel and the screen. By constructing a special extender for the Gadox screen on the camera box, we could significantly decrease this distance, and this together with the lower Gadox screen thickness causes the improvement in the spatial resolution shown in Table 1. We have shown previously that the rest of the imaging system (camera + objective) has significantly lower blur and thus pose no limitation on the spatial resolution in comparison with the aforementioned effects (Zboray et al. 2011a). For quantifying the spatial resolution, in Table 1, the full width at half maximum (FWHM) of the line spread function (LSF) of the imaging system is given. The LSF is obtained by taking the derivative of the edge spread function (ESF) that has been measured using a small, thin rectangular strip of Gd taped directly on the channel. For details on other possible quantifiers for spatial resolution, see, e.g., Smith (1997).

3 Image reconstruction and quality

The imaging is performed in essentially parallel-beam geometry; therefore, it suffices to rotate the channel 180° and record projections in this interval. Furthermore, a three-dimensional reconstruction from the available sets of two-dimensional parallel projections is straightforward, and no cone-beam techniques are necessary: Each horizontal pixel row in the images is processed independently and reconstructed to a cross-sectional image of the channel at the given height (see Fig. 1). Each raw projections image is spot cleaned prior to reconstruction using a median filter to eliminate bright/dark spots caused by gammas/defective pixels, respectively. Furthermore, the raw images are corrected for tilt and are centered with subpixel accuracy for an optimal reconstruction.

The tomographic reconstruction of a set of projections into a stack of cross-sections is done using the filtered back projection (FBP) algorithm (Kak and Slaney 2001). Zboray et al. (2011a) discuss in detail the necessary number of projections and its influence on image quality. We just note that 376 projections in the aforementioned angle range practically always provide a good image quality, for smaller objects occupying about the middle half of the image 226 projections can be already sufficient. The number of projections is a parameter certainly worth optimizing as the available beam time, and thus, the number of experimental runs is usually limited.

The filtering in the FBP procedure is done in the frequency domain using a Hann filter that suppresses higher spatial frequencies decreasing the noise in the reconstructed images and thereby decreases the relative uncertainty of the LFT estimation by about 0.5 % as is shown in Zboray et al. (2011a), with respect to using the so-called Ram–Lak filter, which tends to amplify high frequencies and thereby noise. The frequency response of the two filters and their influence on the spectra of the filtered projection are shown in Fig. 3 for two measurements with different imaging settings. Note that the Hann filter attenuates already in the frequency range where the raw projection still contains information beside noise, especially for the settings with the Gadox screen (see the dashed vertical line). This causes a slight reduction in the spatial resolution of the reconstructed image compared to the Ram–Lak filter. Nevertheless, due to the overall effect of lowering the statistical uncertainty of the LFT, the use of Hann filter should be preferred.

The exposure time per projection for the different experiments has been chosen such that a minimal signal-to-noise ratio (SNR) of at least 30–38 dB is obtained. For such image quality, still feasible exposure times are used as is given in Table 1. Obviously, the actual exposure time to achieve such SNR depends on the choice of screen type and thickness, and also on the flow under investigation: Thicker films need somewhat longer exposure. A typical contrast-to-noise ratio (CNR) between a water film of 2 × 200 μm and the 2 × 3-mm-thick aluminum wall is around 21 dB (the factor 2 comes from penetrating the wall and film twice).

The typical exposure times and the number of projections imply that full tomography an experiment takes several hours; therefore, the results for the LFT obtained here are time-averaged values.

3.1 Referencing

When performing the tomographic reconstruction, the projection images are first normalized by some reference image. In the simplest case, it is an open beam image obtained with no channel in the beam. It is also termed as flat-field correction, and the reconstruction is done on the projection values under angle θ and the lateral distance from the rotation center t, given as:

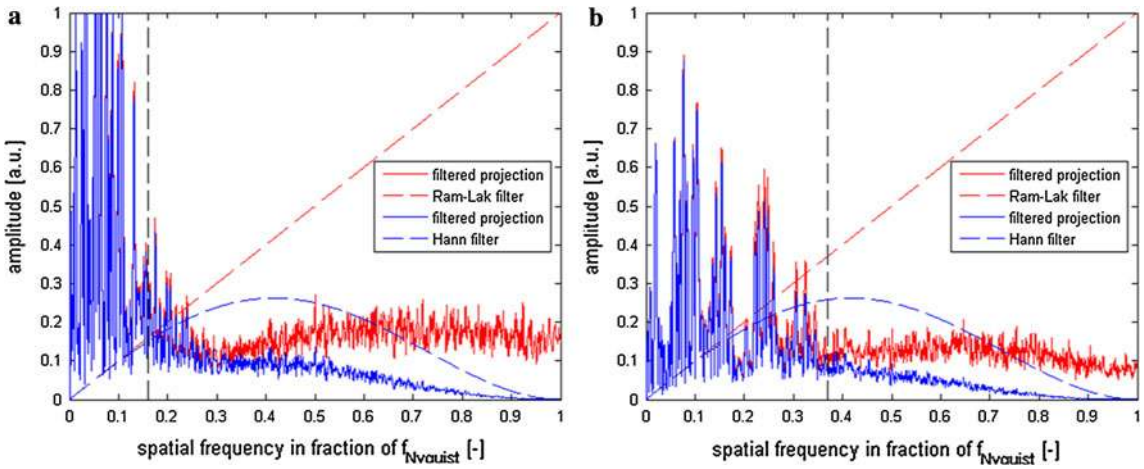

Fig. 3 Frequency response of the filters used in FBP and their influence on the spectra of the projection for a 100 um Li screen (**a**) and for the 20 um Gadox screen (**b**) from Table 1. The *vertical dashed lines* correspond to the spatial resolution limit given in Table 1

$$\mathrm{pr}_{\mathrm{ob}}(\theta,t) = -\ln\left(\frac{(I(\theta,t)-I_{\mathrm{dc}}(t))\cdot D_0/D(\theta)}{I_{\mathrm{ob}}(t)-I_{\mathrm{dc}}(t)}\right) \quad (1)$$

where I is the image intensity taken, and the subscripts ob and dc denote the open beam exposure and dark current values, respectively. The latter is taken without opening the beam and subtracted to compensate for the dark current contribution from the camera. The ratio of the mean pixel value taken over a region outside of the image of the channel denoted by D and D_{o} for the actual and for the open beam exposure, respectively. It serves as a dose correction to compensate for image-to-image fluctuations in the neutron beam intensity or for eventual differences in the exposure times.

Another way is to use as reference the images of the empty channel with no flow taken at the same projection angles as the ones with flow:

$$\mathrm{pr}_{\mathrm{emp}}(\theta,t) = -\ln\left(\frac{(I(\theta,t)-I_{\mathrm{dc}}(t))\cdot D_{\mathrm{emp}}(\theta)/D(\theta)}{I_{\mathrm{emp}}(\theta,t)-I_{\mathrm{dc}}(t)}\right) \quad (2)$$

The latter method enables, in principle, imaging only the water content inside the flow channel and has been shown to produce more accurate results (Zboray and Prasser 2013); therefore, only this will be discussed further.

4 Determining the LFT

It has been shown in Zboray et al. (2011a) that the time-averaged LFT for a fluctuating, wavy liquid film that is always in contact with the channel wall can be calculated as:

$$\mathrm{LFT} = \int_0^{r_{\max}} \varepsilon(r)\mathrm{d}r, \quad (3)$$

where the integral of the time-averaged liquid holdup profile, $\varepsilon(r)$, is taken along a line perpendicular to the channel wall starting at a given point on the channel inner surface ($r = 0$) and $r_{\max}$ is the maximal liquid film height at that point on the wall. $\varepsilon(r)$ is estimated based on the reconstructed images. From the attenuation law, similar to Eq. (1) but ignoring dark current and dose correction for brevity, the projection values under projection angle θ and at distance t from the center of rotation are given as:

$$\begin{aligned}\mathrm{pr}(\theta,t) &= -\ln\frac{I}{I_{\mathrm{ob}}} \\ &= \iint \mu(x,y)\delta(x\ \cos\theta + y\ \sin\theta - t)\mathrm{d}x\mathrm{d}y \end{aligned} \quad (4)$$

where x, y are the lateral coordinates in the tomography plane and μ is the attenuation coefficient. This can be written for two-phase flow in the channel and for an empty channel, respectively, as:

$$\begin{aligned}\mu(x,y) = &(\Sigma_{\mathrm{H_2O}}\varepsilon(x,y) + \Sigma_{\mathrm{air}}(1-\varepsilon(x,y)))F_{\mathrm{ch}}(x,y) \\ &+ \Sigma_{\mathrm{wall}}F_{\mathrm{wall}}(x,y) \end{aligned} \quad (5)$$

$$\mu(x,y) = \Sigma_{\mathrm{air}}F_{\mathrm{ch}}(x,y) + \Sigma_{\mathrm{wall}}F_{\mathrm{wall}}(x,y), \quad (6)$$

where Σ is the macroscopic neutron cross-section. The functions F_{ch} and F_{wall} are equal to 1 inside the channel and in the wall, respectively, and to 0 elsewhere. Substituting Eqs. (5) and (6) into (4), combining them in the fashion of Eq. (2) and by neglecting Σ_{air} being much smaller than $\sum_{\mathrm{H_2O}}$ one obtains:

$$\begin{aligned}\mathrm{pr}_{\mathrm{emp}}(\theta,t) &\approx \iint \Sigma_{\mathrm{H_2O}}\varepsilon(x,y)\delta(x\ \cos\theta + y\ \sin\theta - t)\mathrm{d}x\mathrm{d}y \\ &= R[\Sigma_{\mathrm{H_2O}}\varepsilon(x,y)] \end{aligned} \quad (7)$$

where we dropped F_{ch} as ε is zero everywhere except for the inside of the channel. The right-hand side of Eq. (7) is the well-known Radon transform (Kak and Slaney 2001), denoted by $R[]$, that can be inverted and thus the 2D distribution of the argument, i.e., the image, reconstructed

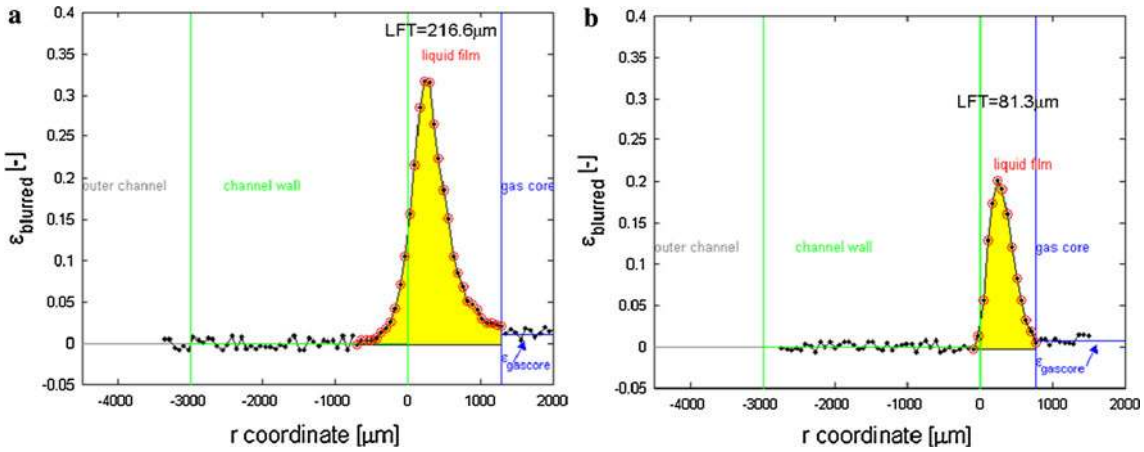

Fig. 4 Typical reconstructed liquid holdup profiles across the liquid film for a thicker film (**a**) and a thinner film (**b**). Note that the profiles blurred differently as different, 100 μm (**a**) and 50 μm (**b**), Li detector screens have been used and thus they extend, e.g., in the region of the channel wall up to a different extent. The *highlighted area* under the curve gives the integral to obtain the LFT. The limits and the gas core average liquid holdup level are also indicated

by analytical or iterative methods. As mentioned above, we use the FBP algorithm. The pixel gray values of the reconstructed image are proportional to the time-averaged liquid holdup value in the channel:

$$p(x,y) = \Sigma_{H_2O}\varepsilon(x,y) \tag{8}$$

As our imaging system is non-ideal, the reconstructed intensity distribution is actually blurred compared to the actual liquid holdup, i.e.,

$$p(x,y) = \Sigma_{H_2O}\varepsilon(x,y) \otimes \mathrm{PSF} = \Sigma_{H_2O}\varepsilon_{blurred} \tag{9}$$

The point spread function (PSF) of the imaging system is the 2D equivalent of the LSF (Smith 1997). Assuming that the convolution Eq. (9) does not alter the integral of the liquid holdup profile across the film but only broadens it, the LFT can be still estimated by integrating $\varepsilon_{blurred}$ according to Eq. (3). This assumption is shown not to hold strictly by Zboray and Prasser (2013); however, the systematic error caused by it is typically very small. Therefore, we keep this assumption and discuss this point briefly below. Note that the actual time-averaged ε distribution is not obtained directly in our measurements. One could try to estimate it from $\varepsilon_{blurred}$ using some deconvolution methods, and we also comment on that in the next section.

Equation (4) holds also for the time-dependent, instantaneous fluctuating values of ε and the intensities I. Using the measured data, we take the logarithm of the ratio of the time-averaged intensities in Eq. (4), which is not identical to averaging the logarithm of the ratio of the time-dependent image intensities, and thus, a statistical bias is introduced due to the nonlinearity of the logarithm with respect to averaging. Based on measurements of the instantaneous LFT by an electrical liquid film sensor (Damsohn 2011; Damsohn and Prasser 2010) under similar two-phase flow conditions in an identical channel geometry as in Fig. 1a, we have estimated this bias using the probability density distribution of the time-dependent LFT and found that it results in about 2 % overestimation of the time-averaged LFT.

The last difficulty in determining the LFT using Eqs. (9) and (3) is to use a proper value of Σ_{H20}. This issue is thoroughly discussed in Zboray and Prasser (2013). We will only summarize the main findings on it below in conjunction with the spectral and scatter effects.

Due to the blurring and broadening, $\varepsilon_{blurred}$ has non-zero values in locations, where ε is zero, e.g., in the channel wall in the vicinity the channel inner surface. Therefore, when applying Eq. (3) for $\varepsilon_{blurred}$, care should be taken in choosing the integration limits. The lower limit is taken where the radial liquid holdup profile first hits the zero value looking from the maximum of the profile toward the channel wall. A typical $\varepsilon_{blurred}$ profile over the liquid film and the integration limits are illustrated in Fig. 4. Regarding the upper integration limit, one should bear in mind that the liquid holdup is not zero in the gas core of the annular flow due to the presence of the droplets. The mean liquid holdup in the gas core, $\varepsilon_{gascore}$, is estimated by averaging over an appropriate region of interest (ROI). The upper integration limit is taken where $\varepsilon_{blurred}$ first reaches $\varepsilon_{gascore}$ moving from the peak of the profile toward the channel interior.

One could, e.g., linearly extrapolate the tail of the $\varepsilon_{blurred}$ profile to get a somewhat more accurate estimate of the zero crossing on the channel wall side. This effect is so tiny that it can be neglected. More important is, however, that the last part of the tail of the profile is lost on the gas core side as it immerses in the "background" given by the gas

core holdup fluctuating around $\varepsilon_{\text{gascore}}$. The missing part of the integral can be easiest approximated by linearly extrapolating this tail of the profile based on its values to the left of the gas core limit (blue vertical line in Fig. 4) to zero as well and taking the area under this extrapolated part. Depending on the flow and the image blur, the underestimation of the LFT caused by omitting this correction can range up to, e.g., 11 % as in the case in Fig. 4a. For dryer annular flows with lower LFT and $\varepsilon_{\text{gascore}}$, the underestimation in the LFT is usually much lower, e.g., 0.9 % in case of Fig. 4b.

Note that our values of spatial resolution and the typical pixel sizes would normally be much too coarse to accurately resolve LFTs around 1–2 pixels or smaller. The image blurring, however, broadens the liquid film profile over a larger number of pixels as illustrated in Fig. 4, improving the resolution of its integral c.f. Eq. (3). Nevertheless, blurring has also an adverse effect on the accuracy of the LFT as will be discussed below in Sect. 5.

This brings up the issue of the limits LFT detection using this technique. The lower limit of the detectable LFT is mainly interesting for very thin films as shown below for the upstream faces of spacer vanes and could be estimated using the following considerations. Taking the individual projection images, the CNR of the liquid film should be reasonable higher than 1. Assuming that the neutron detection (counting) is a Poisson process, we can estimate the noise level for typical number of counts, i.e., average image intensity I_{av}, acquired during the exposures and thus the CNR as:

$$\text{CNR}_{\text{film}} = \frac{(I_{\text{av}} - I_{\text{film}})/I_{\text{av}}}{\sigma_{\text{rel}}(I_{\text{av}})} \cong \frac{1 - \exp(-\Sigma_{\text{H}_2\text{O}}\text{LFT})}{1/\sqrt{I_{\text{av}}}}. \quad (10)$$

Requiring, e.g., a minimal CNR of 1.5, we obtain $\text{LFT}_{\text{min}} = 25$–$30$ μm for the typical exposures times and intensities we use. For a box-car shaped film of that thickness the typical image blurring we have, would result in a peak value in the reconstructed holdup profile of $\varepsilon_{\text{blurred,peak}} \sim 0.08$. The actual time-averaged ε profiles are not box-car-shaped but broader and rather have tails and would give somewhat lower $\varepsilon_{\text{blurred,peak}}$ values for the same LFT. Nevertheless, considering that the maximal $\varepsilon_{\text{gascore}}$ values for the annular flows we examined are always less than 0.02, it can be concluded that the $\varepsilon_{\text{blurred}}$ profile corresponding to LFT_{min} could still be reliably detected above the gas core values fluctuating around $\varepsilon_{\text{gascore}}$.

The maximum detectable LFT can be limited on the one hand by excessive attenuation by the liquid phase and the related beam starvation as cold neutrons are highly sensitive for water. In practice, this starts to pose a severe limit only above some centimeters of LFT. Obviously, if due to the geometry of the setup, multiple liquid films have to be projected through the upper detection limit of the LFT decreases proportionally to the number of films. On the other hand already for 5–10 mms of LFT, strong spectral and scatter effects arise (see Fig. 6). When extreme, these might be difficult to fully compensate for and are discussed in the next section.

Note that though we focus here on determining the LFT, obviously Eqs. (8) and (9) can be also used to determine the time-averaged void (or liquid fraction) in different locations inside the channel or its average over a certain ROI or the full channel cross-section.

5 Image artefacts, spectral and scatter effects

Artefacts always burden tomographic reconstruction in practical situations up to different extent. In our case, these include edge enhancement effects at the edges of the aluminum channel walls (see the surfaces of the reconstructed empty channels in Fig. 1). It is due to beam refraction as at these low energies the corresponding wave lengths are such that cold neutron show noticeable wave behavior. This effect, as is discussed in Zboray et al. (2011a), is most pronounced at the outer surface of the channel wall and does not influence much the LFT determination. Beam starvation artefacts occur typically in the vicinity of highly attenuating structures or regions. When subtle, they appear as halos or shading (called also bloom artefacts in the literature, see, e.g., the vicinity of the corners of the channel in Fig. 5), and when severe, as high-intensity streaks and areas of beam starvation (see, e.g., the dark crossing lines in Fig. 5 in the middle subchannel gap between the two semicircular walls).

Figure 5 shows also the so-called ring artefacts, which are especially pronounced in Fig. 5b and decrease significantly when empty channel referencing is used c.f. Eq. (1). Ring artefacts are caused by the slightly differing characteristics of neighboring detector pixels, including, e.g., "dead" pixels. In both cases, we used a simple moving-averaging algorithm on the sinogram to try to detect and remove/decrease the rings prior to reconstruction. This simple method is relatively efficient in removing the strongest ring artefacts. They, in fact, deteriorate/influence the LFT determination, luckily, however, only locally in limited areas. For details on it, see Zboray et al. (2011a) and in Zboray and Prasser (2013). Note that a volume of literature is dealing with different techniques for reducing this type of artefacts, though with limited success.

The major part of the attenuation of the neutron beam for many materials, e.g., for water, is due to scattering rather than absorption. Scattered neutrons from the sample examined can still reach the detector and contribute to the recorded intensity adding a false contribution to the non-attenuated part of the beam on the detector. Regions with

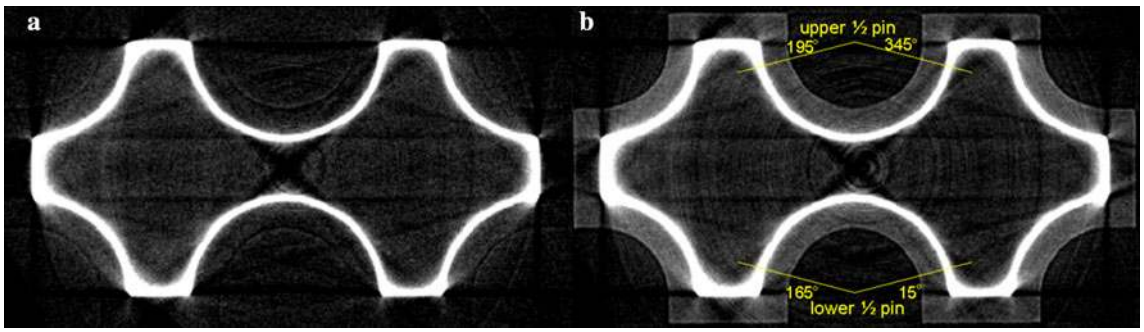

Fig. 5 Reconstructed channel cross-sections using two different referencing: Eqs. (2) and (1) for (**a**) and for (**b**), respectively

high water content, e.g., in the corners of our flow channel or behind thick liquid films (see Fig. 5), have increased scatter contribution resulting in artefacts. Furthermore, there is a scatter contribution to the image from surrounding structural materials (see, e.g., the detector box in Fig. 1) and walls around the imaging setup. This contribution has been measured imaging a "black" neutron absorber (a thick boron block) of similar size as the sample, practically fully blocking the direct beam contribution to the image in the region where the sample is placed. It has been found to be practically constant all over the image, amounting to somewhat less than the dark current contribution. This constant value can be simply added to the dark current intensities in Eq. (1) and (2) to account for it.

The spectral effect is due to using a polychromatic neutron beam (see the spectrum in Kaestner et al. 2011). Strongly attenuating specimen (e.g., thick water films) can cause beam hardening effects, i.e., the mean energy of the neutrons transmitted through it is gradually shifted to higher energies, represented by usually smaller interaction cross-sections, resulting in a lower apparent attenuation (thickness) as the actual one. In the literature, it is also referred as cupping effect. Note that also the energy-dependent sensitivity of the converter screen should be taken into account in this respect.

To try to understand the influence of spectral and sample scatter effects on the LFT and to try to compensate for it, several approaches have been examined. Finally, the best solution turned out to be a direct Monte Carlo (MC) simulation-based approach (Zboray and Prasser 2013). Furthermore, MC simulations enabled gaining a better understanding of the influence of the different imaging parameters and helped to validate our technique and approach to estimate the LFT. The MC simulations of the neutron imaging of the different flow channels have been performed using the general purpose MC code for simulating neutral particle transport MCNP Version 5 (X-5 Monte Carlo Team 2008). Detailed discussion on this study is given in Zboray and Prasser (2013) and for brevity is omitted here, only the most important findings are summarized. First of all, detailed comparison of the MC simulations and measured results revealed certain facts on how to obtain a correct effective macroscopic cross-section for water, $\sum_{H_2O,eff}$, to be used in Eq. (9) to convert image gray values to $\varepsilon_{blurred}$. The true double differential scattering cross-section data must be used in the simulations instead of the default free-gas approximation for scattering. The latter is only appropriate in case of scattering on free atoms not on ones combined to molecules. The binding of the scattering nucleus in molecules (e.g., in water) affects the neutron cross-section and the energy and angular distribution of secondary neutrons, particularly in cold and thermal neutron energy range. Furthermore, modeling the energy dependent detector sensitivity, caused by the energy dependent neutron interaction cross-sections of Li or Gd in the detector screen, is also needed to get a correct value of $\sum_{H_2O,eff}$ for the given imaging setup. Keeping these points in mind, by simulating the actual imaging setup, one can correct for the spectral and scatter effect as is shown in Fig. 6. Based on the explanation of the scatter and spectral effects above, it is clear that in the limit LFT $\rightarrow$ 0, both effects vanish and the larger the LFT is, the stronger are these effects. With other words, as the LFT increases, the value of $\sum_{H_2O,eff}$, that satisfies the attenuation law for the given LFT, is not constant but decreases due to beam hardening and the scattered contribution. A practical way to correct for these effects is to instead of the, $\ln(I_o/I)_{mes}$, a corrected one given as:

$$\ln\left(\frac{I_o}{I}\right)_{corr} = \ln\left(\frac{I_o}{I}\right)_{mes} + \mathrm{LFT}_{mes}\Sigma_{H_2O,eff(\mathrm{LFT}\rightarrow 0)} - \left[\ln\left(\frac{I_o}{I}\right)_{MC}(\mathrm{LFT}_{mes})\right] \quad (11)$$

where

$$\ln\left(\frac{I_o}{I}\right)_{MC}(\mathrm{LFT}_{mes}) = \ln\left(\frac{I_o}{I}\right)_{mes} \quad (12)$$

$\ln(I_o/I)_{MC}$ is the MC simulated attenuation as a function of LFT (the dashed line in Fig. 6). LFT*$\sum_{H_2O,eff}$(LFT $\rightarrow$ 0)

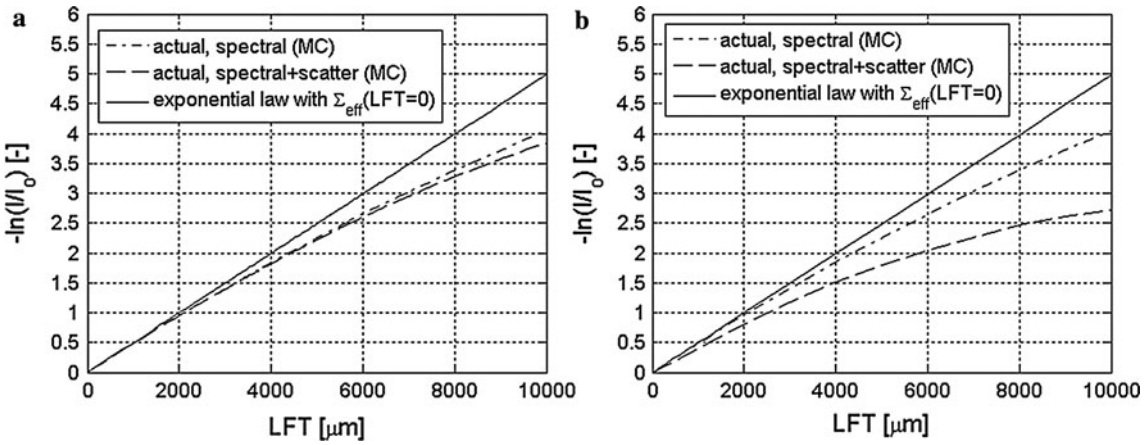

Fig. 6 MC simulation of the attenuation for increasing LFT in the channel for 17 cm (**a**) and for 2.5 cm (**b**) channel-to-detector distances (cf. Table 1). The limiting case obeying the attenuation law for $\sum_{H_2O,eff}(LFT \rightarrow 0)$ is shown by a *solid line*. The other two curves show the actual attenuation of the film with the given LFT if only the spectral effect (*dot-dashed lines*) and if both spectral and sample scatter contributions are taken into account (*dashed lines*)

represents the attenuation of the limiting case of LFT → 0 (the solid line in Fig. 6) and corresponds to the attenuation law satisfied by the hypothetical $\sum_{H_2O,eff}(LFT \rightarrow 0)$. The latter value is determined by extrapolating MC simulation results obtained for gradually decreasing LFTs. The correction is uniquely defined as the attenuation curves in Fig. 6 are monotonic, and it is done pixel wise on all the projection images prior to reconstruction. $\sum_{H_2O,eff}(LFT \rightarrow 0)$ is then used to convert the pixel gray values of the reconstructed image into liquid holdup according to Eq. (9). Note that to get rid of the minus sign in front of the logarithm in the above formulas, the nominator and denominator have been swapped.

Using MCNP, one can distinguish between un-collided and collided contributions in the detector, the former being obviously free of the sample scatter, and it, however, contains the spectral effect (beam hardening). This enables to separate the magnitude of two effects from each other as is shown in Fig. 6. For large channel to screen distances of 17 cm given in Table 1, the spectral effect is larger than the scatter effect. For the small distance of 2 cm, the situation is opposite (compare Fig. 6a, b) and the total correction needed is larger. This is physically plausible, and points out that for a lower blur preferable short channel to screen distance is unfavorable for spectral and scatter artefacts.

Note that in practice, attenuation curves like in Fig. 6 for correcting spectral and scatter effect could be also obtained experimentally, making MC simulations needless, by projecting through the flooded channel and using the known channel cross-section. This projection should be taken under an angle that makes sure that the full interesting LFT range is covered down to very low LFTs to be able to estimate $\sum_{H_2O,eff}(LFT \rightarrow 0)$.

At this point, we refer back to the section on image referencing and point out that one could try to use for referencing the image of the water-filled channel in combination with the empty channel image. It can be shown using Eqs. (4–6) and the counterpart of (5) for the flooded channel, again ignoring dark current and dose correction that taking ratio

$$\frac{R\left[\mathrm{pr}_{\mathrm{empty}}\right]^{-1}}{R\left[\mathrm{pr}_{\mathrm{flooded}}\right]^{-1}} = \frac{R\left[\ln(I/I_{\mathrm{empty}})\right]^{-1}}{R\left[\ln(I_{\mathrm{flooded}}/I_{\mathrm{empty}})\right]^{-1}} = \varepsilon_{\mathrm{blurred}} \qquad (13)$$

gives the distribution of the liquid holdup directly ($R[]^{-1}$ denotes the inverse Radon transformation) and thus the advantage is clearly that no conversion of gray values of the reconstructed image and the quest for $\sum_{H_2O,eff}(LFT \rightarrow 0)$ is needed unlike with Eqs. (8) and (9). However, projection through thick water layers in the flooded channel would cause so excessive beam attenuation that might be unfeasible to do and furthermore it would result in extremely strong spectral and scatter artefacts. This could be still reasonably well corrected as explained above. More importantly, however, due to the blur, the denominator in Eq. (13) is strongly underestimated in the vicinity of the channel inner surface resulting in non-physical liquid holdup values just in the region where the film is. Note that, as idealized MC simulations show, even without blur in the projections the reconstruction of the water-to-wall edge in the flooded channel at the inner channel surface is always smeared out just due to the finite frequency response of the reconstruction method.

By simulation, the whole tomography process by MCNP for liquid films with prescribed thicknesses it was found (Zboray and Prasser 2013) that spectral and scatter corrections of the raw projections is a must to avoid systematic

errors and the omission of them alone is responsible for an up to 5 % underestimation of the LFT. Another systematic effect revealed by the simulations, amounting to 2–4 % underestimation of the LFT, is related to the blur in the projection images. Details are given in Zboray and Prasser (2013) and for brevity, only the two most important effects in this relation are illustrated here. Figure 7 shows a part of a simulated projection profile through the flow channel of Fig. 2a with and without blur (note that the measured LSF has been used to blur the profiles). The blur broadens the peaks/sharp gradients in the projections and strongly decreases their amplitude/slope as we already discussed above. Peaks and gradients occur, where the amount of water to be projected suddenly changes. The blurred, lowered peaks upon back projection give lower contribution to the reconstructed image at the location of the corresponding liquid volume than without blur. The missing part is smeared over the image and can never be fully recovered and is the main reason for the underestimation of the LFT for the blurred images. This shows also that the blurring may preserve the integral value of the individual projection profiles, but our assumption above that the integral of the liquid holdup profile in the reconstructed image is always preserved does not fully hold. The other aggravating effect contributing to the underestimation of the LFT is related to the previous and is also illustrated in Fig. 7: blurred, decreased peaks in the projection profile result also in a smaller spectral correction than for the non-blurred profile. This is due to the fact that the spectral correction is monotonous increasing with the LFT as is shown in Fig. 6a and smaller attenuation implies smaller correction.

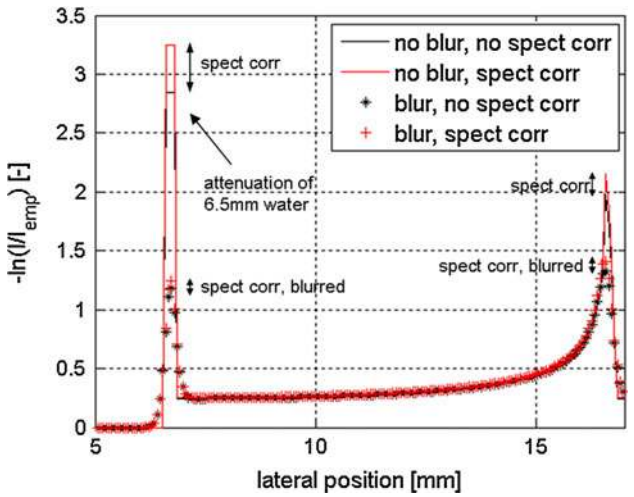

Fig. 7 A section of a simulated attenuation profile of a projection through the channel is illustrated here. The plot shows the same projection profile without and with image blur (solid vs. symbols) and with and without spectral correction. The significant decrease in the sharp peaks due to blur is shown. Furthermore, the smaller spectral corrections obtained for the blurred profiles are illustrated as well

Note that de-blurring (de-convolution) of the images could further improve the estimation of the LFT. We have tested some image deconvolution algorithms, like that of, e.g., the Richardson-Lucy (Richardson 1972; Lucy 1974). However, no really robust way is found to optimize the deconvolution parameters such that all regions of all projection images are equally well corrected. Furthermore, the reconstructions based on deblurred images suffer from quite severe artefacts mainly due to noise enhancements by the deblurring method, which might override any potential improvements by the deblurring. Therefore, we abandon the usage of deconvolution algorithms for the time being, as the bias in the LFT based on the blurred images is limited small values as is shown here. For future experiments, care should be taken when performing LFT measurement by the present technique to minimize the blur of the imaging setup and geometry (thin screens, minimal channel to screen distances, etc.). Nevertheless, trying to find optimal deconvolution techniques—e.g., an interesting constrained least-square method is used by Kramer et al. 2005 for the deconvolution of neutron radiography images—and a correction/compensation for starvation artefacts will be a topic for future investigations.

Compensating for the aforementioned systematic effects is important to minimize the bias of the LFT estimation. The statistical uncertainty of the LFT can always be, in principle, decreased by, e.g., increasing the exposure times; however, systematic effects are very important to be thoroughly analyzed and understood as above to be able to eliminate or alleviate them.

Note that the 2 % overestimation of the LFT caused by the statistical bias due to taking logarithm of the average of fluctuating image intensities mentioned in conjunction with Eq. (4) is partly compensating the aforementioned 2–4 % underestimation caused by the image blur resulting finally in a negative bias $\leq$2 % in the LFT.

6 Results

After thoroughly analyzing the LFT measurement technique, we illustrate its performance in this section through several examples. One of the main goals of our investigations on different fuel bundle models shown in Fig. 2 is to determine the LFT distribution on the surface of the virtual fuel pins inside the channel under different annular flow conditions. We show here as example the results for the channel geometry of Fig. 2a and also shown in Fig. 5. The 2D LFT distributions on the two virtual half fuel pin surfaces are determined. The liquid holdup profile is integrated along radial lines, c.f. Eq. (3), starting from the

center of the fuel pins over an polar angle intervals of 15°–165° and 195°–345° as is shown in Fig. 5b. This is done for the whole FOV that is imaged and also a circumferential distribution of the LFT can be determined. This is shown in Fig. 8b by the blue symbols. The LFT distribution over the polar angle is close to uniform as it is expected and also found by other authors, e.g., Damsohn and Prasser (2010). These LFT values have been averaged axially over the whole height of the FOV. In all experiments for the different channels, if no extra structure is installed inside the channel, we found that the LFT shows no trends as a function of the axial position for a given polar angle, only statistical fluctuations. This indicates a developed annular flow over the FOV. Based on this, the relative uncertainty of the LFT at a polar angle, ϕ, is estimated using the standard deviation (σ) of the LFT calculated at ϕ, over the height of the FOV (y being the axial coordinate) as:

$$\frac{\sigma_{\mathrm{LFT},\phi}}{\mathrm{LFT}_{\phi}} = \frac{\sqrt{\mathrm{var}(\mathrm{LFT}_{\phi}(y))}}{\overline{\mathrm{LFT}_{\phi}(y)}} \tag{14}$$

Depending on the imaging setup and exposure times, we found typical values for the relative uncertainty of the point-wise LFT of 7–11 %. As pointed out above, this could be improved if necessary through decreasing the noise by increasing the exposure times, using higher sensitivity screens or both.

The two-phase flow parameters for the experiments shown in Fig. 8b are summarized in Table 2 in terms of gas and liquid flow rates and superficial velocities defined as:

$$J_{\mathrm{g}} = \frac{\dot{V}_{\mathrm{g}}}{A} \quad \text{and} \quad J_{\mathrm{l}} = \frac{\dot{V}_{\mathrm{l}}}{A} \tag{15}$$

where A is the channel cross-section and $\dot{V}$ is the volumetric flow rate. Further, the gas volume flow fraction is defined as:

$$\beta = \frac{\dot{V}_{\mathrm{g}}}{\dot{V}_{\mathrm{g}} + \dot{V}_{\mathrm{l}}}. \tag{16}$$

As our investigations have been done in the context of annular flow in fuel bundles involving film dryout, another goal was to investigate the influence of functional spacers on the LFT under different flow conditions. Functional spacers besides giving stability to the bundle have vanes that are designed to enhance separation of the droplet and the gas middle of the channel and promote droplet deposition onto the film on the pin surfaces thereby increasing the margin to dryout. A prototypical spacer we tested is shown in Fig. 9. When the spacer is placed inside the channel, the circumferential LFT distribution shows strong variations in terms of the polar angle, mostly increasing but in certain locations also decreasing the LFT as is shown in Fig. 8b. The 2D LFT distributions on the two half pin surfaces in Fig. 8a show even more spectacularly the effect of the spacer. Detailed discussion on the influence of this and another spacer type is given in Zboray et al. (2011a).

Finally, to demonstrate how our technique works for liquid films on small curved, inclined structures, we show some results on resolving the LFT distribution on the surfaces of the vanes of the spacer shown in Fig. 9.

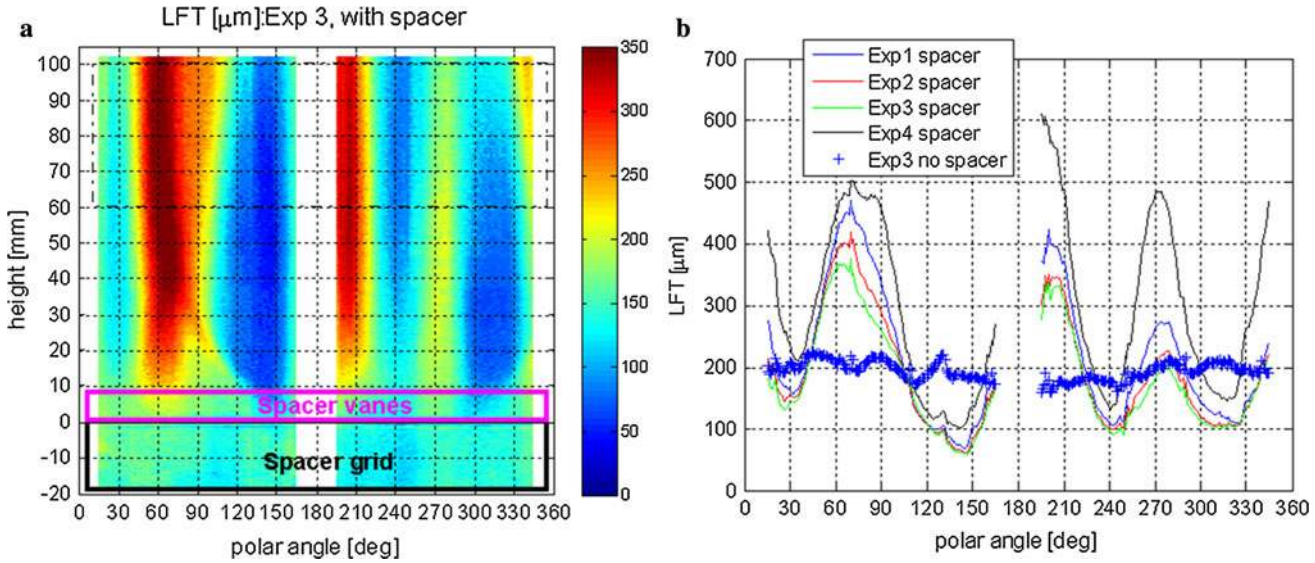

Fig. 8 Contour plot of the LFT distribution on the two half pin surfaces shown in Fig. 5b for Exp 3 (**a**). The region of the spacer grid and the vanes is indicated by the *black and pink rectangles*, respectively. The distribution of the LFT with respect to the polar angle with spacer is shown for the different flow conditions in (**b**), where the LFT has been averaged over the height from 60 to 100 mm above the top of the spacer grid (indicated by the *dashed rectangle*). For comparison, the curve for Exp 3 without spacer in the channel is also shown

Table 2 Two-phase flow parameters for the experiments shown in Fig. 8b

	Air flow (Nm^3/h)	Water flow (l/h)	J_{air} (m/s)	J_{water} (m/s)	$1-\beta$	P_{inlet} (bar)
Exp1	90	878	18.253	0.31	0.0169	1.9
Exp2	90	627	21.52	0.22	0.0103	1.7
Exp3	90	376	26.55	0.13	0.0050	1.55
Exp4	80	1,800	13.39	0.64	0.0459	2.2

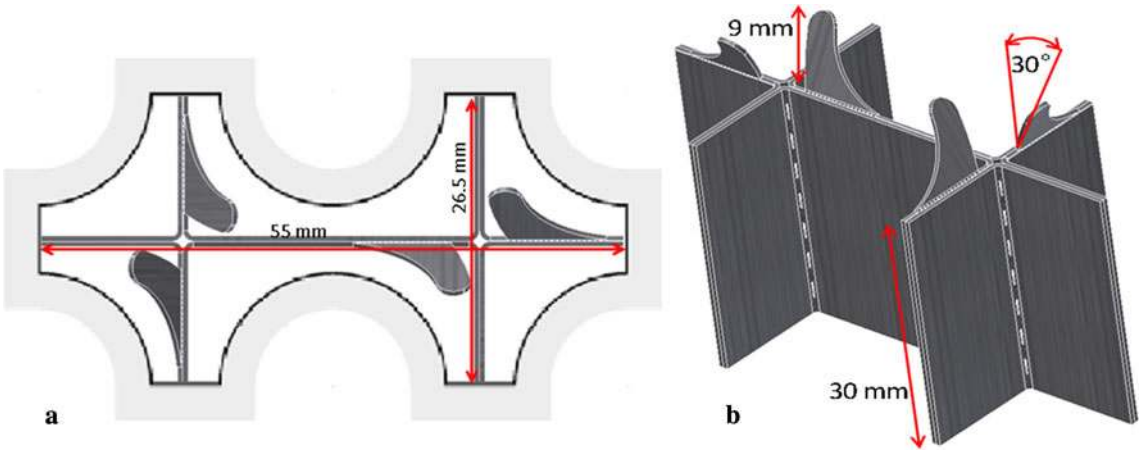

Fig. 9 Cross-sectional view of the channel model with the functional spacer in **a**. A slanted aspect view of the spacer is shown in **b**

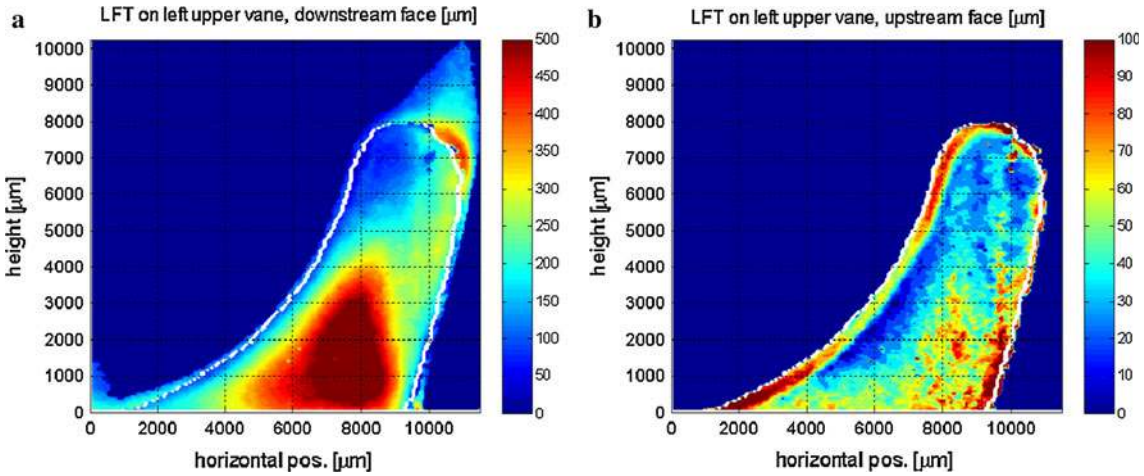

Fig. 10 LFT distribution on the downstream surface (**a**) and on the upstream surface (**b**) of the left-upper vane of the spacer (see Fig. 9a) for Exp2. Note that a side view of the inclined vanes is shown here, therefore their apparent height is lower as is given in Fig. 9b. The white contour of the vane is obtained from imaging the channel without flow

The LFT distributions on the vane for Exp2 are shown in Fig. 10. The lower (upstream) face of the vane holds a significantly thinner film as the upper (downstream) surface. This is obviously due to the direct impact of the gas flow and corresponding strong shear forces on the upstream surface. The LFT shows a strong spatial variation on both surfaces.

The vanes are shown in a side view aspect in Fig. 8, and due to the inclination of the vanes, they appear slightly shorter than the 4.5 mm given in Fig. 2. As we work on a stack of horizontal reconstructed slices, the LFT determined on the inclined vane surfaces is not the film thickness measured perpendicular to the vane surface; therefore, its value has been corrected for this inclination. Spots with

such a low LFT that falls below the lower diction limit discussed in Sect. 5 are assigned with zero LFT.

Note the jet of water running off the vane surface at the tip of the vane in Fig. 10a. This jet is represented by an equivalent LFT in the image for simplicity and is shown exclusively for the downstream face of the vane. 3D rendering of the reconstructed volume around the vane greatly facilitates to see at which proportions from which side of the vane the liquid in the jet originates. Though it is not shown here for brevity, it suggests that it originates to a large fraction from the downstream surface.

7 Conclusions

We have presented a thorough review of an experimental method for measuring liquid film thickness in annular flows using on cold neutron imaging. Cold neutron imaging is a non-intrusive, high-resolution and high-contrast technique. It enables determining accurately the distribution of the time-averaged liquid film thickness in annular flows. The film thickness is obtained with a minimal negative bias ($\leq$2 %). Its statistical uncertainty in our experiments varied between 7 and 11 %, depending mainly on the exposure time and the detector sensitivity. Increasing both of the latter factors, the statistical accuracy can be improved as needed. Imaging with pixel resolution of 60–90 μm has been demonstrated. The method has been optimized, and its performance regarding bias, statistical accuracy, upper and lower detection limits has been thoroughly analyzed using computational tools and measurement results. The influence of imaging artefacts, spectral and scatter effects has been quantified, and correction methods for eliminating or alleviating them have been proposed. Finally, the applicability of the technique has been demonstrated using measurement results taken in the context of investigating annular flows in nuclear fuel bundle models. It could be, however, also applied in other, more general settings with annular flows.

Acknowledgments The authors are very grateful to Dr. Anders Kaestner and to Dr. Eberhard Lehmann of the neutron imaging group of PSI for the opportunity to use the ICON beam line, for their help at performing the measurements and for the useful discussions on the results.

References

Azzopardi BJ (1997) Drops in annular two-phase flow. Int J Multiph Flow 23:1–53

Azzopardi BJ, Zaidi SH (1999) Determination of entrained fraction in vertical annular gas/liquid flow. J Fluids Eng 122:146–150

Crow L (2009) Neutron detectors for imaging. In: Anderson IS, McGreevy RL, Bilheux HZ (eds) Neutron imaging and applications. Springer, Berlin

Damsohn M (2011) Liquid films and droplet deposition in a BWR fuel element. PhD Theses, Diss. ETH No. 19527, Swiss Federal Institute of Technology, ETH Zürich, Switzerland

Damsohn M, Prasser HM (2009a) High-speed liquid film sensor for two-phase flows with high spatial resolution based on electrical conductance. Flow Meas Instrum 20:1–14

Damsohn M, Prasser HM (2009b) High-speed liquid film sensor with high spatial resolution. Meas Sci Technol 20:114001

Damsohn M, Prasser HM (2010) Experimental studies of the effect of functional spacers to annular flow in subchannels of a BWR fuel element. Nucl Eng Des 240:3126–3144

Feldhaus G, Azzopardi BJ, Zeggel W (2002) Annular flow experiments in rod bundles with spacers. Nucl Eng Des 213:199–207

Fore LB, Dukler AE (1995) The distribution of drop size and velocity in gas-liquid annular flow. Int J Multiph Flow 21(2):137–149

Fore LB, Ibrahim BB, Beus SG (2002) Visual measurements of droplet size in gas-liquid annular flow. Int J Multiph Flow 28:1895–1910

Fukano T (1998) Measurement of time varying thickness of liquid film flowing with high speed gas flow by a constant electric current method (CECM). Nucl Eng Des 184:363–377

Han H, Zhu Z, Gabriel K (2006) A study on the effect of gas flow rate on the wave characteristics in two-phase gas–liquid annular flow. Nucl Eng Des 236:2580–2588

Hewitt GF, Hall-Taylor NS (1970) Annular two-phase flow. Pergamon, Oxford

Ishii M, Grolmes MA (1975) Inception criteria for droplet entrainment in two-phase concurrent film flow. AIChE J 21:308–318

Kak AC, Slaney M (2001) Principles of computerized tomographic imaging. Society of Industrial and Applied Mathematics

Kaestner A, Hartmann S, Kühne G, Frei G, Grünzweig C, Josic L, Schmid F, Lehmann EH (2011) The ICON beamline – a facility for cold neutron imaging at SINQ. Nucl Inst Meth A 659:387–393

Kamei T, Serizawa A (1998) Measurement of 2-dimensional local instantaneous liquid film thickness around simulated nuclear fuel rod by ultrasonic transmission technique. Nucl Eng Des 184:349–362

Kardjilov N, Dawson M, Hilger A, Manke I, Strobl M, Penumadu D, Kim FH, Garcia-Moreno F, Banhart J (2011) A highly adaptive detector system for high resolution neutron imaging. Nucl Instrum Methods A 651:95–99

Kok HV, van der Hagen THJJ, Mudde RF (2001) Subchannel void-fraction measurements in a 6x6 rod bundle using a simple gamma-transmission method. Int J Multiph Flow 27:147–170

Kramer D, Zhang J, Shimoi R, Lehmann E, Wokaun A, Shinohara K, Scherer G (2005) In situ diagnostic of two-phase phenomena in polymer electrolyte fuel cells by neutron imaging part A. Experimental, data treatment and quantification. Electrochim Acta 50:2603–2614

Kureta M (2007a) Development of a neutron radiography three-dimensional computed tomography system for void fraction measurement of boiling flow in tight lattice rod bundles. J Power Energy Syst 1(3):211–224

Kureta M (2007b) Experimental study of three-dimensional void fraction distribution in heated tight-lattice rod bundles using three-dimensional neutron tomography. J Power Energy Syst 1(3):225–238

Kureta M, Tamai H, Yoshida H, Ohnuki A, Akimoto H (2008) Development of design technology on thermal-hydraulic performance in tight-lattice rod bundles: V-estimation of void fraction. J Power Energy Syst 2(1):271–282

Lahey RT, Moody FJ (1993) The thermal-hydraulics of a boiling water nuclear reactor, 2nd edn. American Nuclear Society, La Grange Park, IL

Lim EC, Sim CM, Cha JE, Choi YS, Takenaka N, Saito Y, Jun BJ (2005) Measurement of the void fraction in a channel simulating

the HANARO fuel assembly using neutron radiography. Nucl Inst Meth A 542:181–186

Lucy LB (1974) An iterative technique for the rectification of observed distributions. Astron J 79(6):745–754

Misawa M, Tiseanu I, Prasser HM, Ichikawa N, Akai M (2004) Ultrafast X-ray tomography for multi-phase flow interface dynamic studies. Kerntechnik 68(3):85–90

Mishima K, Hibiki T, Saito Y, Nakamura H, Matsubayashi M (1999) The review of the application of neutron radiography to thermal hydraulic research. Nucl Instrum Methods A 424:66–72

Neykov B, Aydogan F, Hochreiter L, Ivanov K, Utsuno H, Kasahara F, Sartori E, Martin M (2005) NUPEC BWR full-size fine-mesh bundle test (BFBT) benchmark, vol. I: Specifications. OECD, Nuclear Energy Agency, NEA No. 6212, ISBN 92-64-01088-2

Richardson WH (1972) Bayesian-based iterative method of image restoration. J Opt Soc Am 62(1):55–59

Smith SW (1997) The scientist and engineer's guide to digital signal processing. California Technical Publishing, San Diego, California

Stahl P, Rudolf von Rohr P (2004) On the accuracy of void fraction measurements by single beam gamma densitometry for gas-liquid two-phase flows in pipes. Exp Thermal Fluid Sci 28:533–544

Takenaka N, Asano H (2005) Quantitative CT-reconstruction of void fraction distributions in two-phase flow by neutron radiography. Nucl Instrum Methods A 542:387–391

Takenaka N, Asano H, Fujii T, Matsubayasi M (1998) Three-dimensional visualization of void fraction distribution in steady two-phase flow by thermal neutron radiography. Nucl Eng Des 184:203–212

Takenaka N, Asano H, Fujii T, Mizubata M, Yoshii K (1999) Application of fast neutron radiography to three-dimensional visualization of steady two-phase flow in a rod bundle. Nucl Instrum Methods A 424:73–76

Trabold TR, Kumar R, Vasallo PF (1998) Annular flow of R-134A through a high aspect ratio duct: local void fraction, droplet velocity and droplet size measurement. KAPL-P-000071, KAPL Atomic Laboratory, Schenectady, New York, 12301

X-5 Monte Carlo Team (2008) MCNP—A general Monte Carlo N-Particle Transport Code, Version 5. LA-UR-03-1987, Los Alamos National Laboratory

Zboray R, Prasser HM (2013) Optimizing the performance of cold-neutron tomography for investigating annular flows and functional spacers in fuel rod bundles. Nucl Eng Des 260:188–203

Zboray R, Kickhofel J, Damsohn M, Prasser HM (2011a) Cold-neutron tomography of annular flow and functional spacer performance in a model of a boiling water reactor fuel rod bundle. Nucl Eng Des 241:3201–3215

Zboray R, Guetg M, Kickhofel J. Barthel F, Sprewitz U, Hampel U, Prasser HM (2011b) Investigating annular flows and the effect of functional spacers in an adiabatic double-subchannel model of a BWR fuel bundle by ultra-fast X-ray tomography. In: Proc. 14th international topical meeting on nuclear thermal-hydraulics (NURETH-14), Toronto, Canada